Journal of Materials Science & Technology xxx (xxxx) 1–12

Contents lists available at ScienceDirect

Journal of Materials Science & Technology

journal homepage: www.elsevier.com



Research Article

# Excellent strength-ductility combination of $Cr_{26}Mn_{20}Fe_{20}Co_{20}Ni_{14}$ high-entropy alloy at cryogenic temperatures

Xuzhou Gao [a, 1], Wei Jiang [a, 1], Yiping Lu [b, *], Zhigang Ding [a], Jizi Liu [c], Wei Liu [a], Gang Sha [c], Tongming Wang [b], Tingju Li [b], Isaac T.H. Chang [d], Yonghao Zhao [a, *]

[a] *Nano and Heterogeneous Materials Center, School of Materials Science and Engineering, Nanjing University of Science and Technology, Nanjing 210094, China*
[b] *Key Laboratory of Solidification Control and Digital Preparation Technology (Liaoning Province), School of Materials Science and Engineering, Dalian University of Technology, Dalian 116024, China*
[c] *Herbert Gleiter Institute of Nanoscience, Nanjing University of Science and Technology, Nanjing 210094, China*
[d] *Metallurgy and Head of Liquid Metal Engineering (LiME) Doctoral Training Centre, Brunel Centre for Advanced Solidification Technology (BCAST), Brunel University London, Uxbridge UB8 3PH, UK*

ARTICLE INFO

*Article history:*
Received 17 June 2022
Received in revised form 20 November 2022
Accepted 7 January 2023

*Key words:*
High-entropy alloys
Strength and ductility
Cryogenic temperature
Twinning
Phase transformation

ABSTRACT

In the present study, a face-centered cubic non-equiatomic $Cr_{26}Mn_{20}Fe_{20}Co_{20}Ni_{14}$ high-entropy alloy (HEA) with a low stacking fault energy of 17.6 mJ $m^{-2}$ was prepared by vacuum induction melting, forging and annealing processes. The recrystallized sample is revealed to exhibit an excellent combination of strength and ductility over a wide temperature range of 4.2–293 K. With decreasing temperature from 293 to 77 K, the ductility and ultimate tensile strength (UTS) gradually increase by 30% to 95% and 137% to 1020 MPa, respectively. At the lowest temperature of 4.2 K, the ductility keeps 65% and the UTS increases by 200% to 1300 MPa, which exceed those published in the literature, including conventional 300 series stainless steels. Detailed microstructural analyses of this alloy reveal a change of deformation mechanisms from dislocation slip and nano-twinning at 293 K to nano-phase transformation at 4.2 K. The cooperation and competition of multiple nano-twinning and nano-phase transformation are responsible for the superior tensile properties at cryogenic temperatures. Our study provides experimental evidence for potential cryogenic applications of HEAs.



## 1. Introduction

Materials used in clean-energy industries, such as liquid natural gas (LNG) and nuclear power, are required to possess high strength, high ductility and toughness, especially at cryogenic temperatures. For example, the LNG is stored at 77 K, and the jacket materials of superconductors in a nuclear reactor operate at 4.2 K. However, body-centered cubic (BCC) and hexagonal close packed (HCP) structural metals and alloys usually experience a ductile-to-brittle transition and become brittle with decreasing temperature to cryogenic atmosphere [1]. Fortunately, materials with face-centered cubic (FCC) structures are even tougher at cryogenic temperatures due to sufficient slip systems [2–4]. It is well known that FCC materials with high stacking fault energies (SFEs), such as Cu and Ni [3,4], deform predominantly by dislocation slips. The cooling down of FCC materials with high SFEs to cryogenic temperature can lead to the followings: (i) decreased thermal activation volume of dislocation slip for plastic deformation, which results in the reduction of mean free path of dislocation slip and the increase of flow stress and strain hardening rate [4,5]; (ii) increased Peierls barrier height, i.e., a higher stress is required to drive dislocations over the Peierls barrier [4]; (iii) suppressed dislocation dynamic annihilation at grain boundaries and within grains due to the weakened thermally-activated cross-slip and climb [6]. The above reduced activation volume and dislocation annihilation as well as enhanced Peierls barrier make dislocation slip difficult, and increase dislocation storage capability and strain hardening ability in the FCC materials at cryogenic temperatures.

The FCC alloys with low SFEs are also reported to have high ultimate tensile strength (UTS) and ductility. For example, 316 stainless steel has outstanding ductility and UTS at 4.2 K (49% and 1680 MPa) and 77 K (56% and 1312 MPa) [7]. Similarly, the ductility and UTS of 304 stainless steel at 77 K are 42% and 1521 MPa, respectively. The ductility and UTS of high-Mn steel at 77 K are 67% and 1403 MPa, respectively [8,9]. The high strength and ductility in FCC alloys with low SFEs are attributed to extra deformation mechanisms involving twinning and phase transformation [9]. Twinning produced extra twin boundaries (TBs) and phase-transformation produced extra phase interfaces, which lead to dynamically accumulating dislocations and hardening during deformation, so-called twinning-induced-plasticity (TWIP) and transformation-induced plasticity (TRIP) effects [10,11]. Thus, over the past several decades, 300 series austenitic stainless steels

* Corresponding authors.
*E-mail addresses:* luyiping@dlust.edu.cn (Y. Lu), yhzhao@njust.edu.cn (Y. Zhao).

[1] These authors contributed equally to this work.

https://doi.org/10.1016/j.jmst.2023.01.023
1005-0302/© 20XX

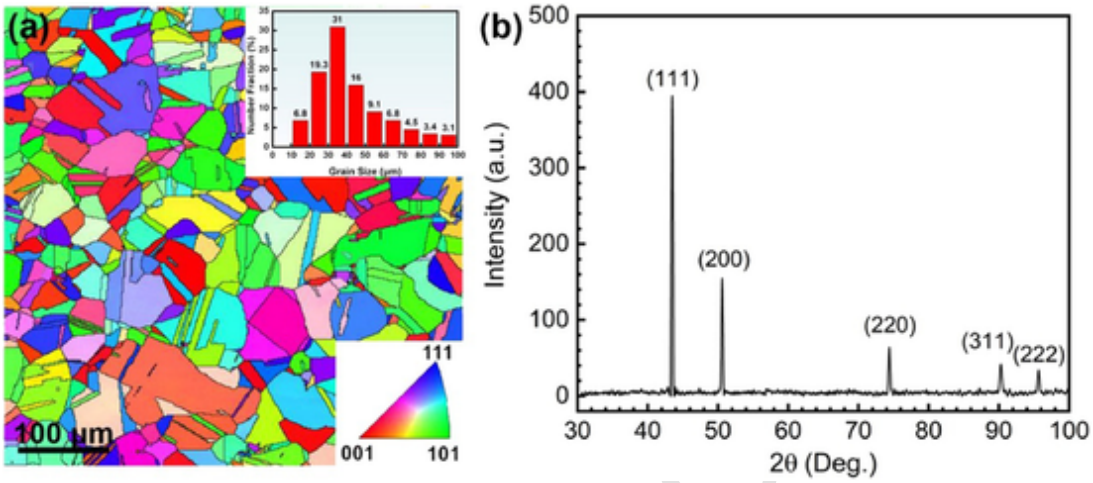


**Fig. 1.** Initial microstructures of the hot-forged and annealed $Cr_{26}Mn_{20}Fe_{20}Co_{20}Ni_{14}$ HEA sample. (a) EBSD crystal orientation map. The upper right inset is statistical grain size distribution. (b) The XRD pattern revealing the single-phase FCC structure of the annealed $Cr_{26}Mn_{20}Fe_{20}Co_{20}Ni_{14}$ HEA.

and high-Mn steels were mainly used in cryogenic industries due to their desirable strength and ductility.

Since emerging at 2004, high-entropy alloys (HEAs), or multi-component alloys, containing at least four principal elements in equal or near equal atomic ratios, open a completely new research field for designing new materials with exceptional cryogenic properties [12–15]. For example, an excellent combination of ductility and strength at 77 K has been reported for single phase FCC CoCrFeMnNi HEA (eg. ductility and UTS of 77% and 1280 MPa) [2] and CoCrNi medium-entropy alloy (MEA) (eg. ductility and UTS of 90% and 1311 MPa) [16], due to the TWIP and TRIP effects. Thus, HEAs and MEAs have potential applications at cryogenic temperatures [2,16–19].

Lowering SFEs can introduce TWIP and TRIP effects that are beneficial to high strength and high ductility of FCC materials. First-principles electronic structure calculations reveal that the SFEs of HEAs can be reduced by tailoring the atomic ratios of individual components [20,21]. For instance, the SFE of CrMnFeNiCo HEA is calculated as approximately 25.5–27.3 mJ $m^{-2}$, and that of $Cr_{26}Mn_{20}Fe_{20}Co_{20}Ni_{14}$ HEA is as low as 3.5 mJ $m^{-2}$ [20]. Therefore, in this study, we selected the $Cr_{26}Mn_{20}Fe_{20}Co_{20}Ni_{14}$ HEA with extremely low SFE as a model material to study its mechanical properties and deformation mechanisms at a wide temperature range of 4.2–293 K. Detailed characterization of microstructures are provided to understand the microstructure-mechanical properties relationship of the investigated HEAs.

## 2. Experiments

### 2.1. Materials

The alloy ingot with a nominal composition of $Cr_{26}Mn_{20}Fe_{20}Co_{20}Ni_{14}$ was prepared from commercially pure elements (Co, Ni: 99.9 wt%; Mn, Cr, Fe: 99.5–99.6 wt%). The BN crucible was heated to 873 K to remove the water vapor and then was putted into the vacuum induction melting furnace together with raw elements. The furnace chamber was first evacuated to $8 \times 10^{-9}$ MPa and then backfilled with high-purity argon gas to reach $6 \times 10^{-2}$ MPa. An IRTM-2CK infrared pyrometer was employed to monitor the temperature with an absolute accuracy of ± 2 K. The pouring temperature was 1823 K and approximately a 2.5 kg of ingot was obtained with a length of 220 mm, an upper inner diameter of 62 mm and a bottom inner diameter of 50 mm. The HEA was re-melted twice to ensure homogeneity. The ingot was hot-forged and subsequently annealed at 1273 K for 8 h to obtain a homogeneous structure.

### 2.2. Tensile tests

Dog-bone shaped specimens with a diameter of 3 mm and a gauge length of 18 mm were cut from the annealed ingot via electrical discharge machining and CNC turning lathe. All tensile tests were performed on an MTS-SANS CMT5000 universal testing machine with contacting strain gages at the Key Laboratory of Cryogenics, Technical Institute of Physics and Chemistry, Chinese Academy of Sciences (TIPC, CAS). Tensile tests of the $Cr_{26}Mn_{20}Fe_{20}Co_{20}Ni_{14}$ HEA were carried out at various temperatures, including room temperature (293 K), in a dry ice-alcohol mixture (203 K), liquid nitrogen (77 K), liquid neon (20 K), and liquid helium (4.2 K) with a strain rate of $1 \times 10^{-3}$ $s^{-1}$. The surface temperatures of tensile specimens were measured by thermodetector. For each temperature, at least three tensile tests were conducted.

### 2.3. Microstructural characterization

Chemical homogeneity of the HEA was investigated via atom probe tomography (APT) using a Local Electrode Atom Probe (CAMECA LEAP 4000X Si). The APT specimen was prepared by a standard two-stage electro-polishing, which is first in an electrolyte of 30% perchloric acid and 70% glacial acetic acid at 12 V, and second in an electrolyte of 5% perchloric acid and 95% 2-butoxyethanol at 15 V at room temperature. Reconstruction and visualization of the APT data were performed using the CAMECA Visualization and Analysis Software (IVAS 3.6.8) package. X-ray diffraction (XRD) analysis was performed with a Bruker-AXS D8 Advance X-ray diffractometer equipped with Cu-Kα radiation source. Electron back scattering diffraction (EBSD) analysis was conducted via a high-resolution field emission Carl Zeiss-Auriga-45-66 scanning electron microscope (SEM). EBSD specimens were electropolished in an electrolyte containing 10 vol% perchloric acid and 90 vol.% acetic acid. Under the applied voltage of 20 V, a shiny mirror-like surface can be achieved for the sample within 30 s by the electropolishing process. Furthermore, transmission electron microscope (TEM) observations were conducted in an FEI-Tecnai $G^2$ 20 S-TWIN microscope operated at 200 kV. The high-resolution transmission electron microscope (HRTEM) analysis was conducted in Titan G2 60-300 microscope operated at 300 kV. The TEM specimens were prepared by electro-polished in an electrolyte containing 10% perchloric acid, 20% glycerol, and 70% methanol at 253 K via a twin jet polishing system.

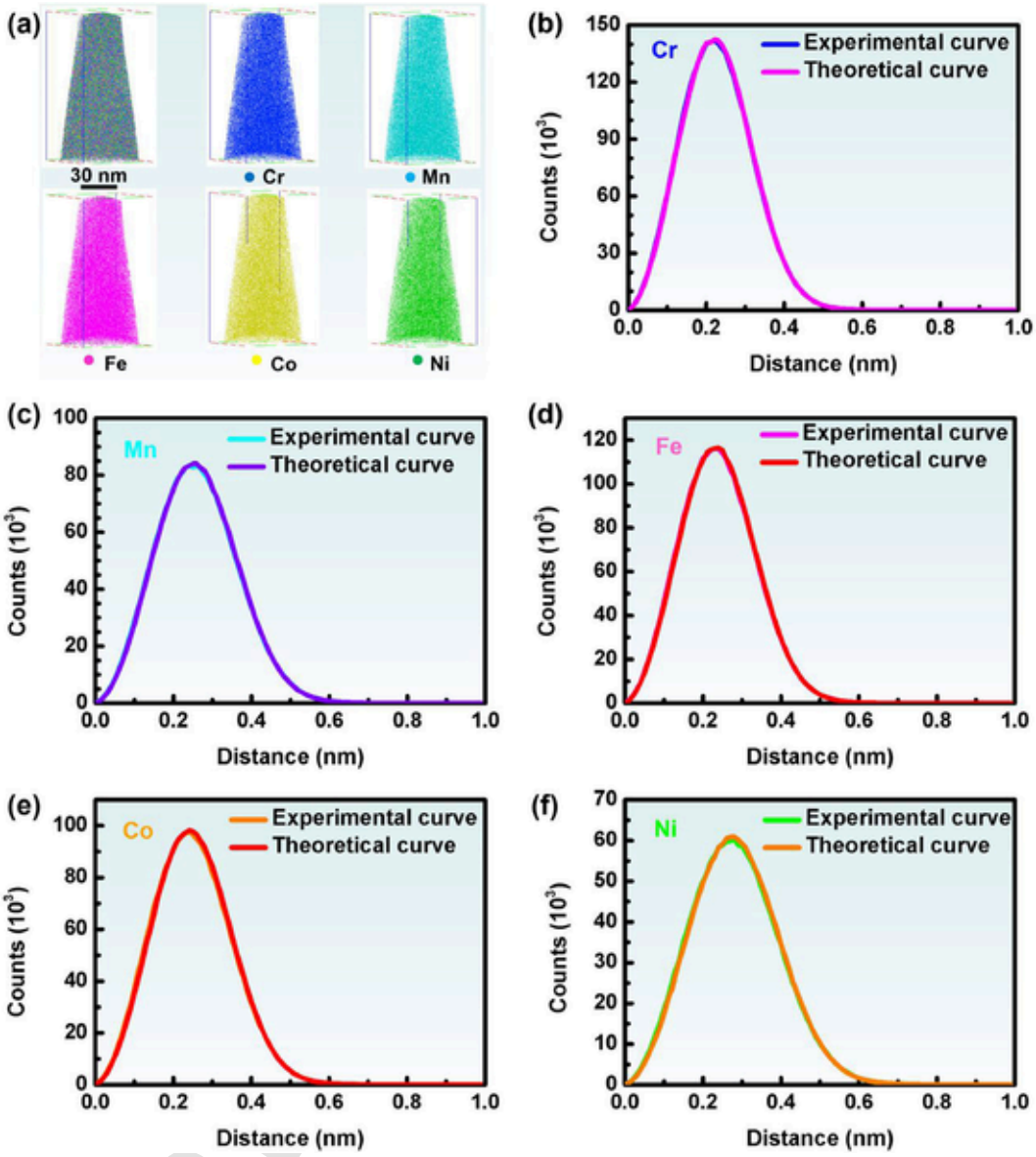


**Fig. 2.** Compositional distribution of the hot-forged and annealed $Cr_{26}Mn_{20}Fe_{20}Co_{20}Ni_{14}$ HEA sample by APT. (a) Combined and individual Cr, Mn, Fe, Co, and Ni atom maps of a 3-D reconstructed volume. (b–f) Nearest neighbor distribution analyses of Cr, Mn, Fe, Co, and Ni in the analyzed volume of the HEA sample with reference curves when the element atoms in the volume are in a random distribution.

## 3. Results

### 3.1. Initial microstructures and compositional distribution

As shown in Fig. 1(a), the annealed $Cr_{26}Mn_{20}Fe_{20}Co_{20}Ni_{14}$ HEA has fully recrystallized microstructure with grain sizes ranging from 10 to 100 μm and an average grain size of 47 μm. The XRD pattern in Fig. 1 (b) reveals a single-phase FCC structure. The compositional homogeneity of the annealed sample was analyzed via APT. The 3D atom maps of a reconstructed volume and the corresponding nearest neighbor distribution analyses in Fig. 2 show the overlap of the experimental curve with the theoretical curve for each element, indicating a uniform and random solid solution without any nano-precipitates or elemental segregations in the HEA.

### 3.2. Tensile properties

Fig. 3(a) shows the engineering stress-strain curves of the $Cr_{26}Mn_{20}Fe_{20}Co_{20}Ni_{14}$ HEA at different temperatures. The detailed mechanical properties are listed in Table 1. As shown in Fig. 3(a) and Table 1, the yield strength (YS), UTS and ductility of the HEA at 293 K are 145 MPa, 430 MPa and 73%, respectively. With temperature decrease to 77 K, the YS, UTS and ductility increase simultaneously to 450 MPa (210% increment), 1020 MPa (137% increment), and 95% (30% increment), respectively. The simultaneous improvement in the low-temperature strength and ductility of the $Cr_{26}Mn_{20}Fe_{20}Co_{20}Ni_{14}$ HEA exceeds those of CrMnFeCoNi HEA but comparable with those of CrCoNi MEA [2,16]. Further decrease of temperature leads to improvement of strength but decline in ductility. At the lowest temperature of 4.2 K, the YS and UTS further increase to 660 MPa (355% increment) and 1300 MPa (200% increment), respectively, while the ductility decreases to 65%. Furthermore, it is noted that the tensile curves of the $Cr_{26}Mn_{20}Fe_{20}Co_{20}Ni_{14}$ HEA exhibit obvious serrations at 20 and 4.2 K.

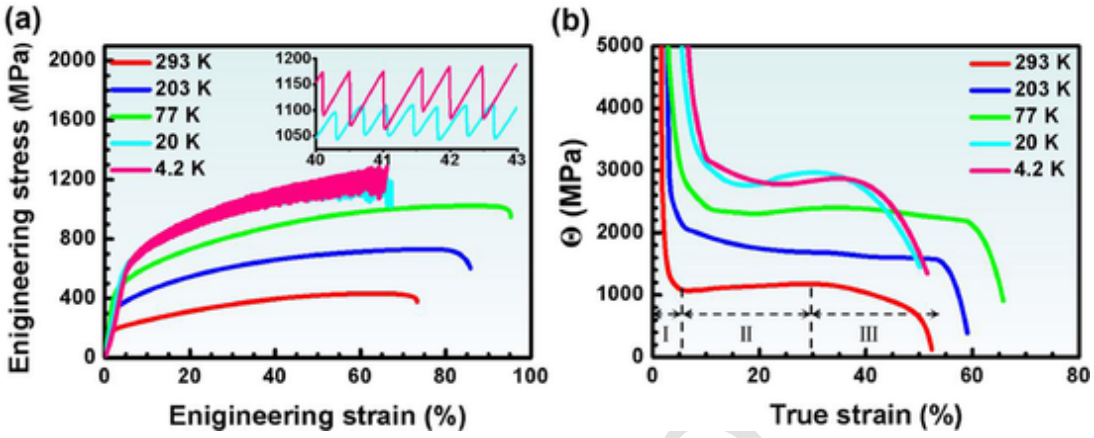


**Fig. 3.** (a) Tensile engineering stress-strain curves tested at different temperatures. The inset shows the serration behaviors at 20 and 4.2 K. (b) Strain hardening rate Θ versus true strain at different temperatures. Three stages could be distinguished, as marked along the black dashed line.

**Table 1**
Lists of the YS, UTS and ductility of the $Cr_{26}Mn_{20}Fe_{20}Co_{20}Ni_{14}$ HEA at different temperatures.

| | Temperature (K) | | | | |
|---|---|---|---|---|---|
| | 293 | 203 | 77 | 20 | 4.2 |
| YS (MPa) | 145 | 355 | 450 | 575 | 660 |
| UTS (MPa) | 430 | 730 | 1020 | 1209 | 1300 |
| Ductility (%) | 73 | 86 | 95 | 66 | 65 |

The stress fluctuation amplitude gradually increases from 8 to 162 MPa with increasing strain.

The strain hardening rates ($\Theta = \partial\sigma/\partial\varepsilon$, where $\sigma$ denotes the true stress, $\varepsilon$ denotes the true strain) at different temperatures are shown in Fig. 3(b). Regardless of temperature, the five strain hardening rate curves exhibit three distinct stages, containing the significant drop of Θ (stage I), the steady-state Θ (stage II) and the further decreases of Θ (stage III). It is worth noting that the stage I extends with decreasing temperature. Strain hardening exponent, *n*, simulated by the Hollomon equation ($\sigma = K\varepsilon_p^n$, where $K$ and $\varepsilon_p$ are the strength coefficient and the true plastic strain, respectively) can be used to evaluate the strain hardening capability. As shown in Fig. 4 and Table 2, the *n* values increase from 0.45 to 0.69 with decreasing temperature from 293 to 4.2 K, comparable to those of stainless steels [10].

Fig. 5 summarizes the UTS and ductility of present HEA and other materials at 4.2 K and 77 K, respectively [2-9,16,22–39]. As shown in Fig. 5(a), at 4.2 K, most metals and alloys exhibit the strength-ductility paradox between UTS and ductility, such as Cu, Al, Ti alloys, etc. However, the $Cr_{26}Mn_{20}Fe_{20}Co_{20}Ni_{14}$ HEA exhibits superior combination of ductility (65%) and UTS (1300 MPa), and the ductility exceeds that of the conventional 316 stainless steel (49%) [7]. At 77 K, the $Cr_{26}Mn_{20}Fe_{20}Co_{20}Ni_{14}$ HEA has the better ductility, comparable to that of CoCrNi MEA [4,5,16,38,39].

### 3.3. Deformation and strengthening mechanisms at room temperature

Detailed TEM characterization was performed to reveal the underlying deformation mechanisms of the $Cr_{26}Mn_{20}Fe_{20}Co_{20}Ni_{14}$ HEA at different temperatures. Figs. 6 and 7 show the TEM micrographs and the corresponding selected area electron diffraction (SAED) patterns of samples tested at 293 K. At a true strain of 2%, a few dislocations and long SFs are observed (Fig. 6(a)). As shown in Fig. 6(b) and (c), a great quantity of planar dislocation arrays and some multiple {111} slip traces are observed at the true strain of 6%, indicating strong planar dislocation slip in the initial deformation stage. Besides, SFs are also found frequently (Fig. 6(c)). With the true strain increase to 22%, deformation twins are observed, as shown in Fig. 6(d). With further increasing plastic strain to fracture (49%), numerous primary deformation twins, secondary deformation twins, and even tertiary twins are observed, which refine the coarse-grained matrix into nano-scale twin lamellae with thickness of tens of nano-meters (Fig. 6(e)). High density dislocations are observed within the twin lamellae (Fig. 6(f)).

HRTEM method was used to analyze the SF in the tensile-fractured sample with a strain of 49% at 293 K. As shown in Fig. 8(a), the SF is formed by the dissociation of an extended 1/2<110> dislocation into two 1/6<112> partial dislocations. Fig. 8(b) and (c) display several SFs with widths ranging from 7.9 to 21.8 nm, indicating there is a large scattering of SF width measured by HRTEM. Fig. 8(d) shows the distribution of measured SF width from 38 SFs in the $Cr_{26}Mn_{20}Fe_{20}Co_{20}Ni_{14}$ HEA and the average SF width is 13.6 nm. The SFE can be determined by the equation [40]:

$$\gamma = \frac{\mu b_p^2}{8\pi d}\frac{2-\nu}{1-\nu}\left(1-\frac{2\nu\cos 2\beta}{2-\nu}\right) \quad (1)$$

where $\gamma$ is the SFE, $\mu$ is the shear modulus, approximately equal to 79.3 GPa [41], $b_p$ is the magnitude of Burgers vector, $d$ is the SF width, $\nu$ is the Poisson's ratio, $\beta$ is the angle between the dislocation line and the Burgers vector of the dislocation (0° for the screw dislocation and 90° for the edge dislocation). At 293 K, the SFE of the $Cr_{26}Mn_{20}Fe_{20}Co_{20}Ni_{14}$ is calculated as 17.6 mJ $m^{-2}$, which is larger than the result by first-principle calculation (3.5 mJ $m^{-2}$) but lower than the measured SFE of CrMnFeCoNi HEA (30 ± 5 mJ $m^{-2}$) by TEM [41].

### 3.4. Deformation and strengthening mechanisms at cryogenic temperatures

Fig. 9 presents the microstructures of the $Cr_{26}Mn_{20}Fe_{20}Co_{20}Ni_{14}$ HEA at cryogenic temperatures and Fig. 10 displays the corresponding SAED patterns. At 203 K, some long SFs and nano-scale twins are frequently observed. As shown in Fig. 9(a), SFs on two sets of {111} planes intersect with each other and spread uniformly within the grains. Based on the statistical distribution of SF width from 32 SFs, the average SF width and SFE are measured as 17.5 nm and 13.7 mJ $m^{-2}$ at 203 K, as shown in Fig. 11(a). Furthermore, some deformation-induced nano-twins and a small number of HCP laths are also observed, as shown in the inset in Fig. 9(b) and the corresponding SAED patterns in Fig. 10(a–c). Fig. 12(a) and (b) further illustrates the nano-twins and HCP laths by HRTEM, respectively. As shown in Fig. 12(b), the HCP laths are sandwiched between matrix and twins. The lattice parameters $a$ and $c$ of the deformation-induced HCP phase are measured as 2.56 and 4.13 Å, respectively. According to the SAED patterns in Figs. 9(b) and 12(c), the HCP laths exhibit a consistent orien-

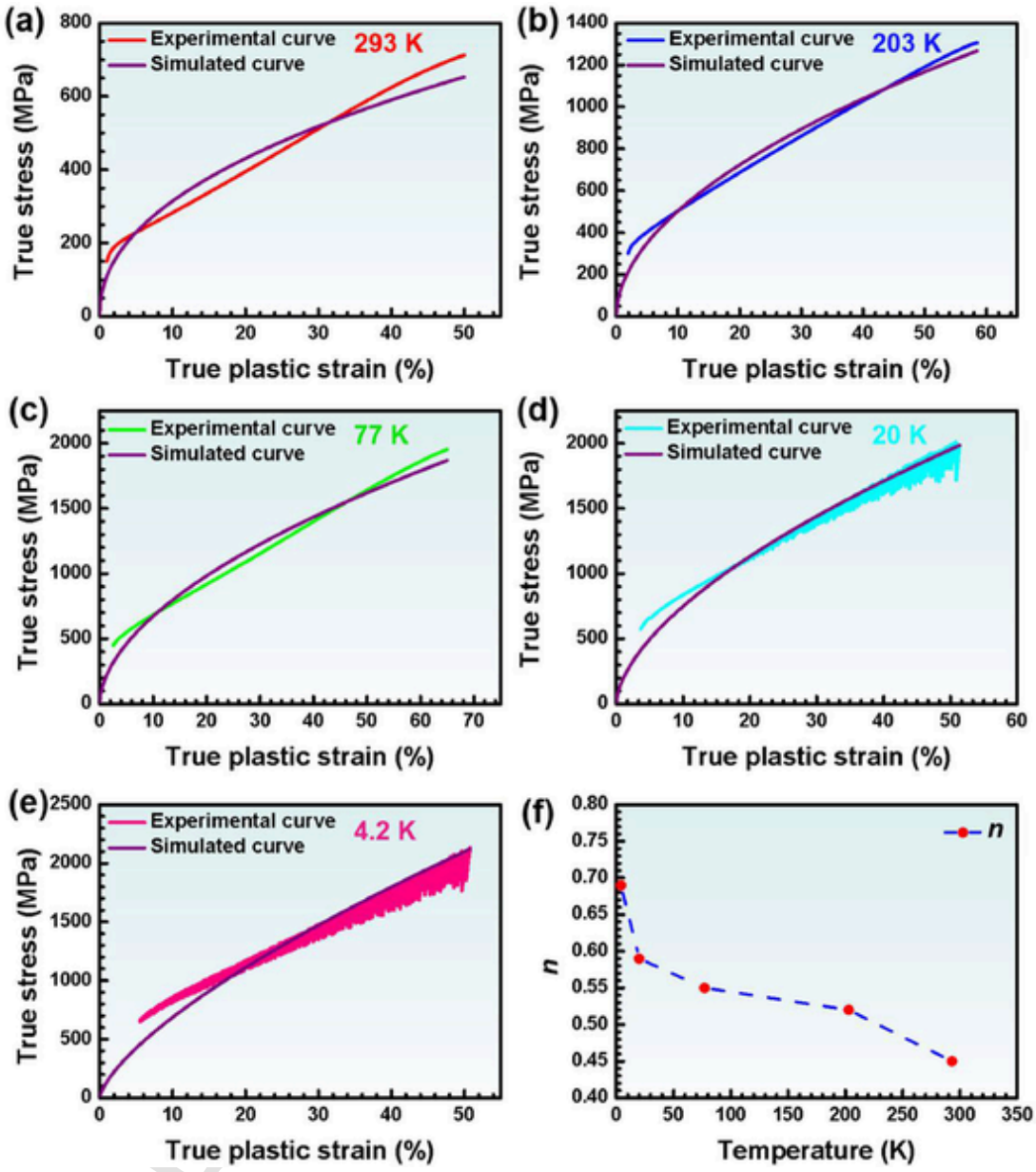


**Fig. 4.** (a–e) Experimental true stress versus true plastic strain curves and simulated curves by Hollomon equation of the $Cr_{26}Mn_{20}Fe_{20}Co_{20}Ni_{14}$ HEA at different temperatures. (f) Variations of $n$ with temperatures.

**Table 2**
Lists of the simulated values of the strain hardening exponent, $n$, and the strengthening coefficient $K$ from the Hollomon equation.

| | Temperature (K) | | | | |
|---|---|---|---|---|---|
| | 293 | 203 | 77 | 20 | 4.2 |
| $K$ (MPa) | 895 | 1677 | 2363 | 2948 | 3394 |
| $n$ | 0.45 | 0.52 | 0.55 | 0.59 | 0.69 |

tation relationship with the matrix as $(000\text{-}1)_{HCP} \parallel (\text{-}111)_{FCC}$ and $[2\text{-}1\text{-}10]_{HCP} \parallel [110]_{FCC,}$ and share the same {111} habit planes with the coherent boundaries of the nano-twins [42].

At temperature of 77 K, lower SFE enhances the SF activities. As shown in Fig. 11(b), the average SF width is measured as 25.7 nm from 21 SFs and the corresponding SFE is calculated as 9.9 mJ $m^{-2}$ at 77 K. As shown in Fig. 9(c), numerous projections of SFs overlapped on one type of {111} planes and formed the discontinuous fringe contrast are observed in the fractured HEA specimen. Furthermore, the interactions between three pairs of parallel {111} faults form a rhombic hexahedron (termed as "stacking-fault parallelepipeds" [43]), as shown in the inset B in Fig. 9(c). Additionally, the content of the HCP phase increases as compared to that at 203 K. As shown in Fig. 9(d), the primary deformation nano-twins and nano-HCP lamellae, are cut by the secondary type (inset C in Fig. 9(d)) and form the parallelogram shaped intersection structure (marked by the yellow parallelogram).

At temperatures of 20 and 4.2 K, SFs and twins are seldom observed, and the single HCP phase transformation govern the plastic deformation, indicating the SFEs are further lowered. Unfortunately, the statistical distribution of SF width and SFEs at 20 and 4.2 K couldn't be provided by the HRTEM measurements. As shown in Fig. 9(e) and (f), the HCP bundles are observed in fractured HEA specimen, containing several HCP lamellae with a thickness of approximately 5 nm. Another observed microstructural feature is the severe collision between the HCP bundles from different slip directions. As shown in area "D" in Fig. 9(e) and the magnified image in Fig. 9(g), two HCP bundles collide together

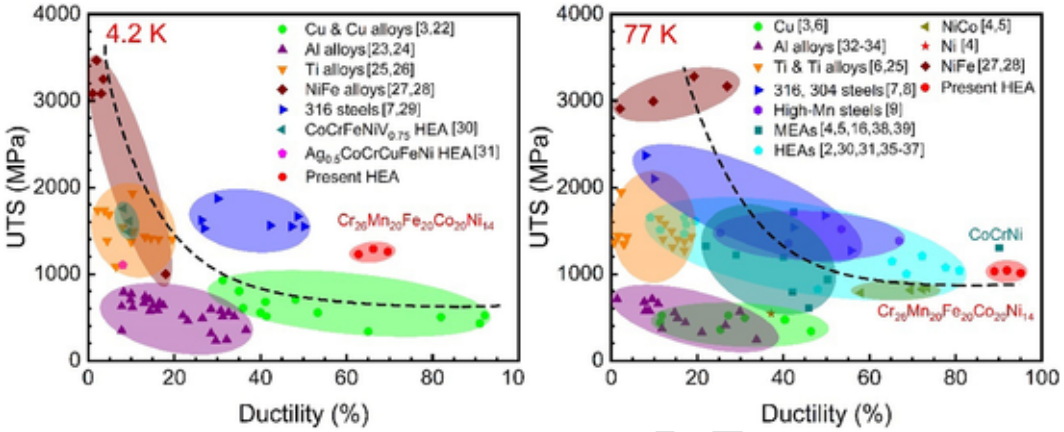


**Fig. 5.** Ultimate tensile strength (UTS) versus ductility of Cu, Al, Ti, Ni, NiFe, and NiCo alloys, 316, 304 and high-Mn steels, MEAs and HEAs at 4.2 K (a) and 77 K (b), respectively. The dashed black lines were draw to schematically show the trade-off relationship between the UTS and ductility.

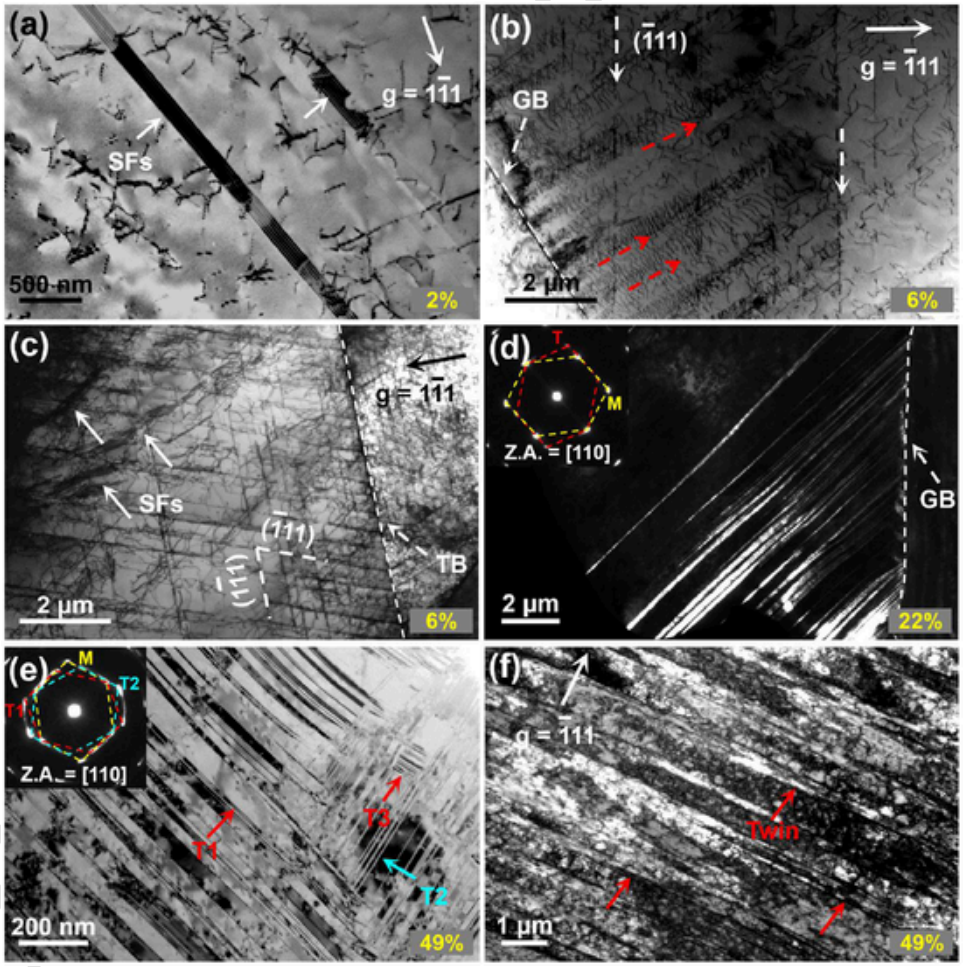


**Fig. 6.** TEM micrographs of the $Cr_{26}Mn_{20}Fe_{20}Co_{20}Ni_{14}$ HEA with different *g* vectors and tensile true strains at 293 K. The fully labelled selected area electron diffraction (SAED) patterns are shown in Fig. 7. (a) SFs are indicated by white arrows. (b) Parallel dislocation arrays and (-111) slip traces are indicated by dotted red and white arrows, respectively. (c) Two sets of {111} slip traces and SFs are indicated by white dashed lines and solid arrows. (d) [110] zone axis (Z.A.) dark field TEM micrograph showing deformation twin. The inset is SAED pattern of matrix "M" and twin "T". (e) [110] zone axis bright field TEM micrograph showing multiple twinning systems "T1","T2" and "T3". (f) High-density and homogeneously-distributed dislocations.

and causes a slight deviation of 4.3° from the original slip direction of the upper HCP bundle, generating small-angle GBs. The nano-HCP lamellae at the intersecting region are divided into nano-grains (marked by yellow dotted lines) with large-angle misorientation to the original slip direction (marked by red dotted arrows). As shown in the lower left region denoted as "E" in Fig. 9(e) and the magnified image in Fig. 9(h), a thin HCP bundle cut through a thick HCP bundle. The thin HCP bundle also breaks into nano-grains with large-angle misorientation. Besides, a single HCP bundle crosses another HCP bundle, giving a

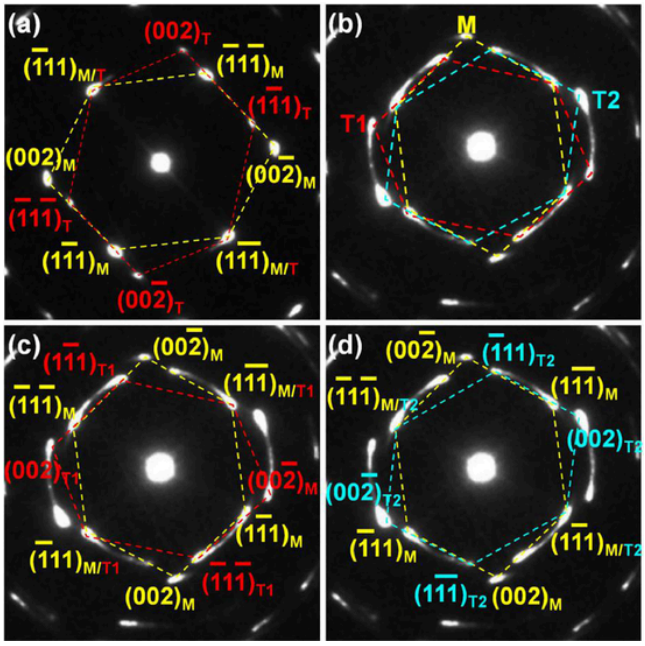


**Fig. 7.** (a) Fully labelled SAED pattern under [110] zone axis in Fig. 6d. The matrix and twin are marked as "M" and "T" respectively. (b) The SAED pattern under [110] zone axis of matrix (marked as "M") and twins on two twinning systems (marked as "T1" and "T2") in Fig. 6e. (c) Fully labeled SAED pattern of "M" and "T1" in (b). (d) Fully labeled SAED pattern of "M" and "T2" in (b).

6.4° deflection of slip direction at 4.2 K, as shown in the SAED in Fig. 9 (f).

XRD experiments were performed on the tensile samples of $Cr_{26}Mn_{20}Fe_{20}Co_{20}Ni_{14}$ HEA at different temperatures. As shown in the Fig. 13(a), the diffraction peaks representing the (10-11) crystallographic plane for HCP phase are observed first at 203 K, corresponding to the results from TEM (Fig. 9). With decrease of temperature, the intensity of (10-11) diffraction peak enhances, indicating the increase of volume fraction of HCP phases. According to the literature [44], the volume fraction of HCP phases can be quantitative calculated by the equation:

$$V_\varepsilon = \frac{1/n\sum_{j=1}^{n} I_\varepsilon^j / R_\varepsilon^j}{1/n\sum_{j=1}^{n} \frac{I_\gamma^j}{R_\gamma^j} + 1/n\sum_{j=1}^{n} I_\varepsilon^j / R_\varepsilon^j} \quad (2)$$

where $n$ is the number of examined peaks, $I$ is the integrated intensity of the diffraction peak, $R = \frac{1}{\upsilon}F^2P\left(\frac{1+\cos^2 2\theta}{\sin\theta\sin 2\theta}\right)e^{-2M}$ is the material scattering factor, $\upsilon$ is the volume of the unit cell, $F$ is the structure factor, $P$ is multiplicity factor, $e^{-2M}$ is temperature factor, $\theta$ is diffraction angle. As shown in the Fig. 13(b), the volume fraction of HCP phases in the sample at 203 K is approximately 4.7%. The volume fraction of HCP phases increases with temperature decrease, and is approximately 30% at 4.2 K.

## 4. Discussions

### 4.1. Temperature dependence on strain hardening rate

As shown in Fig. 3(b), all the HEA samples exhibit three distinct stages with broad steady-state, which is different from the monotonic decrease in conventional polycrystalline metallic materials. The fast drop of strain hardening rates in stage I at a given temperature corresponds to the conventional transition from elastic to dislocation-slip-dominated plastic deformation [45]. At 293 K, the mobile unit dislocations in dislocation arrays and the fast movement of SFs are responsible for the lower Θ value in stage I (Fig. 6(a–c)) [43]. While the hysteretic Θ drop or the extended stage I with decreasing temperature is resulted from the increase of critical resolved shear stress (CRSS) for unit dislo-

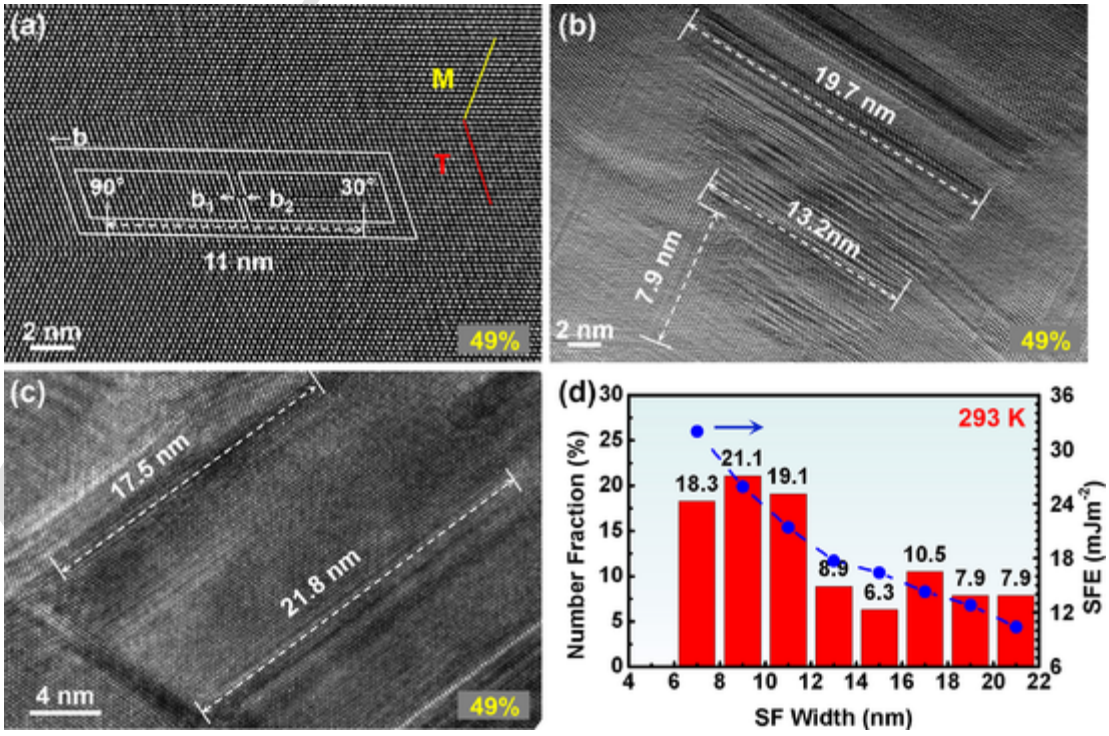


**Fig. 8.** [110] zone axis HRTEM images of the tensile-fractured $Cr_{26}Mn_{20}Fe_{20}Co_{20}Ni_{14}$ HEA with $\varepsilon$ = 49% at 293 K. (a) HRTEM image revealing a SF was formed from the dissociation of an extended 1/2<110> dislocation to two 1/6<112> partial dislocations. (b,c) HRTEM image showing massive SFs with width ranging from 7.9 to 21.8 nm. (d) Statistical distribution of SF width and SFE at 293 K.

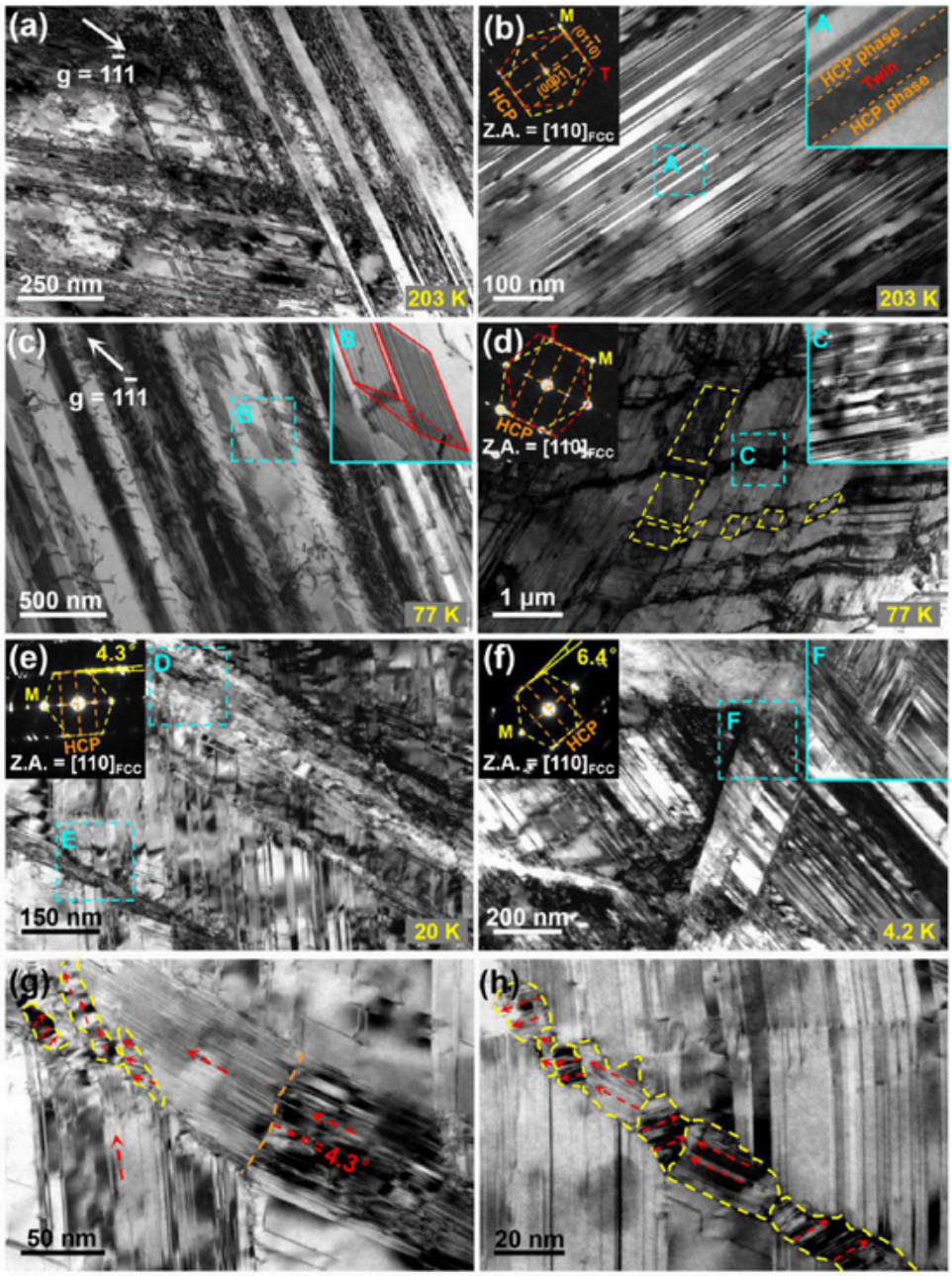


**Fig. 9.** Postmortem bright-field TEM images of the tensile fractured $Cr_{26}Mn_{20}Fe_{20}Co_{20}Ni_{14}$ HEA at different temperatures. The fully labelled SAED patterns are showed in Fig. 10. (a) SFs intersection structure. (b) Deformation twins and nano-HCP phase as well as the SAED pattern under $[110]_{FCC}$ zone axis. (c) SFs parallelepipeds. (d) The intersection structure of nano-twin-HCP composite lamellae on the two slip systems and the SAED pattern under $[110]_{FCC}$ zone axis. (e, f) Severe intersection of HCP phase and the $[110]_{FCC}$ zone axis (Z.A.) SAED pattern. (g, h) Magnification of regions D and E, respectively, and shows the nano-grains (denoted by a yellow dotted line) with large-angle misorientation to the original slip direction (denoted with red dotted arrows).

cation [5]. In stage II, the steady-state Θ is due to additional strengthening and hardening effects from deformation twinning and/or transformation, as shown in the TEM results above. The steady-state Θ delays the necking and finally enhances the uniform elongation and overall ductility. It is worth noting that the strain range of the stage II first increases with temperature decreasing from 293 K to 77 K, and then decreases with temperature decrease to 4.2 K, corresponding to the evolution of ductility in Fig. 3(a). At 293 K (Fig. 6(d)), twin lamellae typically act as effective obstacles to impede the motion of dislocations, especially for those with slip direction not parallel to the twin lamellae [46,47]. The deformation twinning dynamically increases the capacity of dislocation accumulation and contributes to the steady-state Θ in stage II. At lower temperatures (203 K and 77 K), the density of twins increases and phase transformation occurs, introducing more twin lamellae and phase boundaries. Therefore, the samples at 203 K and 77 K possess higher strain hardening rate and broader steady-state II. While the $Cr_{26}Mn_{20}Fe_{20}Co_{20}Ni_{14}$ HEA exhibits obvious serration behaviors at 20 and 4.2 K. The similar serration behaviors are widely reported in the Al-Mg alloys [48,49], TWIP steels [10,50] and metal glass [51], resulting from the repeated pinning-breaking dislocation activity by the diffusing-solutes, twinning and shear band. The authors believe that the deformation twinning results in the serration behaviors in $Al_{0.5}$CoCrCuFeNi HEA [52] at low temperature (7–9 K). For presently studied $Cr_{26}Mn_{20}Fe_{20}Co_{20}Ni_{14}$ HEA deformed at 20 and 4.2 K, the serration behaviors are attributed to the propagation and interaction of the HCP lamellae (Fig. 9(e-h)). The tensile stress was released when the HCP

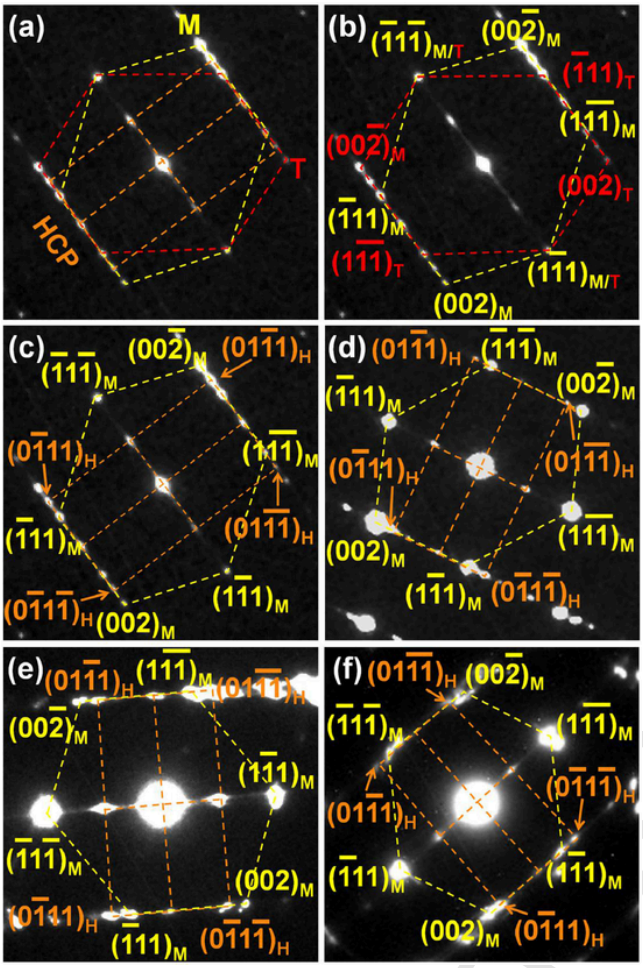


**Fig. 10.** (a) The SAED pattern under $[110]_{FCC}$ zone axis of matrix (marked as "M") and twin (marked as "T") as well as HCP phase in Fig. 9(b). (b) Fully labeled SAED pattern of "M" and "T" in (a). (c) Fully labeled SAED pattern of "M" and HCP phase (marked as "H") in (a). (d,e,f) Fully labeled SAED pattern of "M" and "H" in Fig. 9(d, e, f), respectively.

lamella propagated smoothly while it was accumulated when the propagation of the HCP lamella was blocked. The severe serration behaviors result in plastic instability and premature fracture of $Cr_{26}Mn_{20}Fe_{20}Co_{20}Ni_{14}$ HEA at 20 and 4.2 K (Fig. 3(a)). As shown in Fig. 6(f), dislocations distribute and accumulate homogeneously within twin and matrix lamellae. This means that the saturation of dislocations, twins and phase transformation result in further decreases of Θ in stage III [45].

### 4.2. Temperature dependence on mechanical properties

As shown in Fig. 3(a), the yield strength, ultimate tensile strength of the $Cr_{26}Mn_{20}Fe_{20}Co_{20}Ni_{14}$ HEA all increase with decreasing temperature from 293 K to 4.2 K. While the ductility increases with temperature decrease from 293 K to 77 K and then decreases with temperature decrease from 77 K to 4.2 K. The evolutionary trend of strength is in accordance with that of CrMnFeCoNi HEA. The superior combination of strength and ductility in CrMnFeCoNi HEAs are ascribed to the enhanced dislocation motion and earlier start of twinning at cryogenic temperatures [2,53]. While the strengthening and toughening mechanisms of the $Cr_{26}Mn_{20}Fe_{20}Co_{20}Ni_{14}$ HEA have some difference due to the lower SFE (17.6 mJ $m^{-2}$ at 293 K). According to literature [54], the deformation mechanisms of FCC materials can be summarized as a function of SFE: (i) slip deformation of unit dislocations when SFEs exceed 60 mJ $m^{-2}$; (ii) twinning deformation when SFEs are in the range of 20–60 mJ $m^{-2}$; (iii) transformation-induced deformation when SFEs are lower than 20 mJ $m^{-2}$. For the $Cr_{26}Mn_{20}Fe_{20}Co_{20}Ni_{14}$ HEA sample at 293 K, the deformation mechanism changes from dislocation slip at low strain level ($\varepsilon < 6\%$) to deformation twinning at medium to high strain ($\varepsilon > 22\%$) (Fig. 6).

The SFE is also affected by the temperature, and decreases by 20%–30% when the temperature decreases from 293 to 77 K [55]. The SFE of the $Cr_{26}Mn_{20}Fe_{20}Co_{20}Ni_{14}$ HEA at 203 K and 77 K are 13.7 mJ $m^{-2}$ and 9.9 mJ $m^{-2}$, respectively (Fig. 11). Compared to 293 K, the further decrease of SFE at cryogenic temperatures enhances activity of SF and nanoscale twinning. As shown in Fig. 9(a) and (c), SF parallelepipeds are observed. Within the 3D parallelepipeds fault structure, three individual SFs on three unparallel {111} planes act as the faces of the hexahedron. The interactions between the two partial dislocations on conjugated {111} planes form immobile Lomer-Conttrell dislocation locks. The 3D SF structure and the Lomer-Conttrell dislocation locks are effective in blocking of dislocation motion, thereby leading to a significant strain hardening effect. Deformation twinning, by constantly generating new boundaries and reducing the mean free path of dislocations during plastic deformation ("dynamic Hall–Petch"), produces a high degree of strain hardening and a significant increase in the UTS. Moreover, twinning can provide an additional deformation mode to accommodate plastic deformation. The three-dimensional twin networks offer multiple pathways for dislocation motion along the TBs and dislocations can cross-slip from one TB to another through the "overpass" mechanism constructed by the intersected TBs [56].

AT cryogenic temperatures, the reduced CRSS of the HCP phase-transformation makes the transformation easier [57,58] and induces TRIP effects in $Cr_{26}Mn_{20}Fe_{20}Co_{20}Ni_{14}$ HEA (Fig. 9). The formed HCP lamellar structures are very effective barriers for dislocation slip since the transmission of edge-component dislocations into the HCP phase would require the activation of $<\boldsymbol{c}>$ or $<\boldsymbol{c}+\boldsymbol{a}>$ dislocation with a component along [0001] [57]. The $<\boldsymbol{c}>$ or $<\boldsymbol{c}+\boldsymbol{a}>$ dislocation typically exhibits extremely high CRSS in HCP materials, especially at low

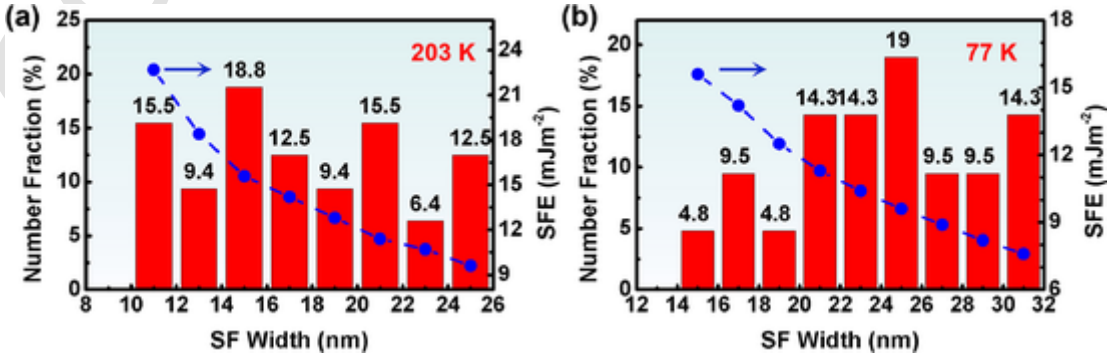


**Fig. 11.** Statistical distributions of SF width and SFE at 203 K (a) and 77 K (b), respectively.

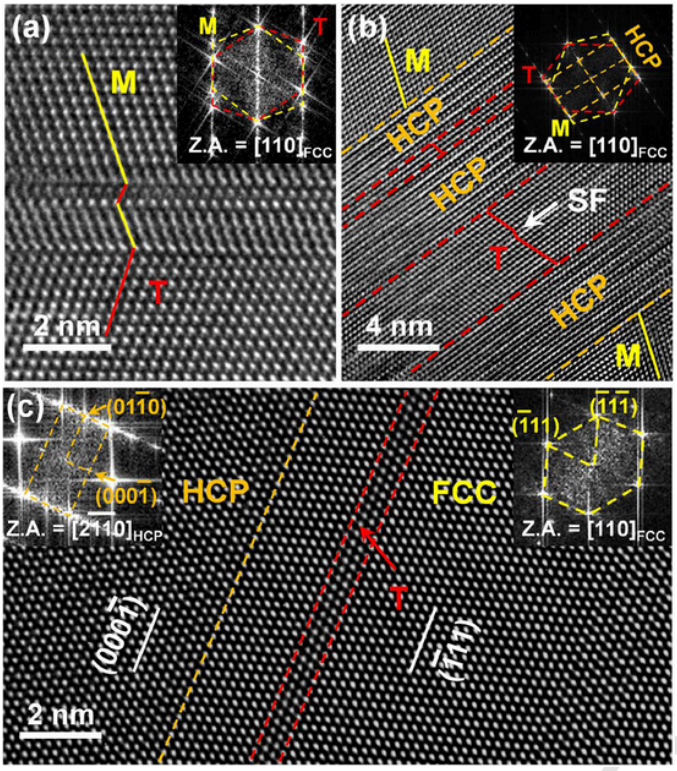


**Fig. 12.** HRTEM images on $[110]_{FCC}$ zone axis of the tensile-fractured $Cr_{26}Mn_{20}Fe_{20}Co_{20}Ni_{14}$ HEA at 203 K. The insets show the corresponding fast Fourier transform (FFT) patterns. (a) Deformation nano-twin with three atomic layers. (b) nano-scale HCP laths sandwiched between matrix and twins. (c) HRTEM image showing the $[2\text{-}1\text{-}10]_{HCP}$ || $[110]_{FCC}$ relationship. The HCP phase shares the same {111} habit planes with the coherent twin boundaries.

temperatures. Besides, the nano-HCP laths are mainly formed in the presence of nano-twins, leading to the formation of nano-twin-HCP composite lamellae (Figs. 9(b) and 12). The nanocomposite lamellae offer an optimal partition of strain and stress, and decrease the possibility of damage nucleation due to their elastic compliance. Briefly, the combination of enhanced SFs, TWIP and TRIP effects contribute to excellent work hardening, preventing the early onset of necking instability. Thus, the $Cr_{26}Mn_{20}Fe_{20}Co_{20}Ni_{14}$ HEA possesses the simultaneous increase in strength and ductility at 203 K and 77 K (Fig. 3(a)).

At temperature of 20 K and 4.2 K, the HCP phase transformation dominates the plastic deformation. As shown in Fig. 9(e-h), the HCP bundles and severe collision between the HCP bundles from different slip directions are observed, leading to microstructure refinement. The dynamic phase transformation, the high densities of phase boundaries and the grain refinement contribute to higher strength (1300 MPa) at 4.2 K (Fig. 3(a)). However, the severe serrations at 4.2 and 20 K caused by frequent FCC→HCP phase transformation result in plastic instability and premature fracture of the $Cr_{26}Mn_{20}Fe_{20}Co_{20}Ni_{14}$ HEA. Thus, the ductility decreases obviously at 20 K and 4.2 K (Fig. 3(a)).

### 4.3. FCC→HCP transition mechanism

HRTEM was employed to discover the formation mechanisms of HCP phase in terms of dynamics at atomic scale in the $Cr_{26}Mn_{20}Fe_{20}Co_{20}Ni_{14}$ HEA. Fig. 14(a) illustrates the transient phase boundary (denoted by the orange dotted line) between the FCC and HCP phases deformed at 20 K. A typical 1/6<112> Shockley partial dislocation is observed and demonstrate that the atomic formation mechanisms of the HCP phase from the FCC phase is alternate SF generation, as schematically represented in Fig. 14(b). Nine atomic layers in the FCC matrix with an atomic packing order of ABCABCABC are inspected. As shown in Fig. 14(b), when an atomic layer is displaced by a Shockley partial dislocation, an SF is introduced with a stacking sequence of CABCABABC, namely a thin HCP phase lamella with four atomic layers of ABAB. When another Shockley dislocation moves on the alternate (not adjacent) close-packed plane, the double alternating SFs exhibit an atomic packing sequence corresponding to BCABABABC, namely an HCP phase with six atomic layers. Therefore, the HCP phase transformation of the $Cr_{26}Mn_{20}Fe_{20}Co_{20}Ni_{14}$ HEA at cryogenic temperatures is realized via alternating SF generation.

From thermodynamics, the phase transformation depends on the difference in Gibbs free energies between the FCC and HCP phases. The molar Gibbs free energy difference $\Delta G^{FCC\rightarrow HCP}$ shows a positive relationship with the SFE, $\gamma$, and is expressed as [59,60]:

$$\Delta G^{FCC\rightarrow HCP} = \frac{\gamma - 2\sigma^{FCC\rightarrow HCP}}{2\rho} \quad (3)$$

$$\rho = \frac{4}{\sqrt{3}a^2 N} \quad (4)$$

where $\sigma^{FCC\rightarrow HCP}$ is the coherent FCC-HCP interfacial energy (10 ± 5 mJ $m^{-2}$) [59,61], $\rho$ is the planar packing density (moles/area) of a close-packed plane {111}, $a$ is the lattice constant of the FCC phase (3.58 Å) and $N$ is the Avogadro's number ($6.02 \times 10^{23}$). As shown in Fig. 15, the values of $\Delta G^{FCC\rightarrow HCP}$ decrease with temperature, and are in a range marked as red shadow area. Obviously, the $\Delta G^{FCC\rightarrow HCP}$ (> 80%) mostly perform as negative values and the fraction of negative

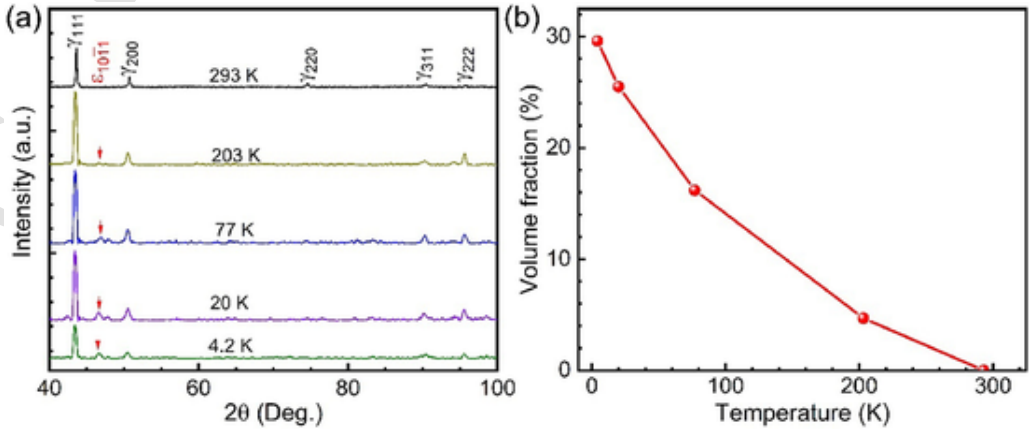


**Fig. 13.** (a) The XRD patterns of the $Cr_{26}Mn_{20}Fe_{20}Co_{20}Ni_{14}$ HEA samples after tensile at different temperatures. (b) Evolution of the volume fraction of HCP phases with temperature.

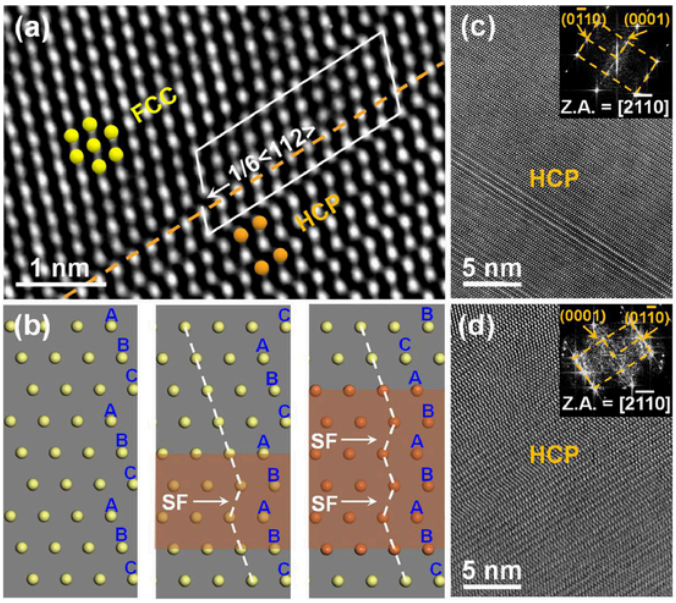


**Fig. 14.** (a) [110] zone axis HRTEM images of the $Cr_{26}Mn_{20}Fe_{20}Co_{20}Ni_{14}$ HEA tested at 20 K. Phase boundary is denoted by the orange line between FCC and HCP. (b) Schematic atomic formation mechanisms of the HCP phase from the FCC phase via alternate SF generation. (c, d) The [2-1-10] zone axis HRTEM images of HCP phase at 20 and 4.2 K, respectively. The insets show corresponding FFT patterns.

values increases with decreasing temperature. When the temperature dropping to 77 K, the highest value of $\Delta G^{FCC\rightarrow HCP}$ is as low as -1.67 J $mol^{-1}$, i.e. the negative fraction reach 100%. The negative value suggests that the formation energy of HCP phase is lower than that of FCC phase, and the HCP phase is more stable than FCC phase. The calculations based on the density-functional theory (DFT) also revealed that the formation energy of HCP structure is lower than that of FCC structure in CrCoNi MEA [62] and CrMnFeCoNi HEA [63] at 0 K, indicating the HCP structure is stable at cryogenic temperature. Therefore, the decrease of SFE with decreasing temperature induces the decrease of $\Delta G^{FCC\rightarrow HCP}$, promoting the HCP phase transformation in the $Cr_{26}Mn_{20}Fe_{20}Co_{20}Ni_{14}$ HEA, especially at cryogenic temperatures. According to Fig. 15, it is a scientific inference that the lower SFE decreases the values of $\Delta G^{FCC\rightarrow HCP}$, enhancing the HCP phase transformation. By extrapolation, $\Delta G^{FCC\rightarrow HCP}$ at 20 and 4.2 K can be deduced and the SFEs can be calculated to be 7.12~7.35 mJ $m^{-2}$ at 20 K and 6.1-6.87 mJ $m^{-2}$ at 4.2 K, respectively. As shown in Fig. 14(c) and (d), the higher densities of HCP phases at 20 and 4.2 K confirm the above inference.

## 4. Conclusions

In this work, a $Cr_{26}Mn_{20}Fe_{20}Co_{20}Ni_{14}$ HEA was prepared and studied in terms of the microstructures and mechanical properties as a function of temperature from 293 to 4.2 K. Through systematic characterization of microstructures and investigation of strengthening mechanisms, we elucidate the microstructure-mechanical properties relationship of the $Cr_{26}Mn_{20}Fe_{20}Co_{20}Ni_{14}$ HEA. The main conclusions are as follows:

(1) The $Cr_{26}Mn_{20}Fe_{20}Co_{20}Ni_{14}$ HEA with low-SFE (17.6 mJ $m^{-2}$ at 293 K calculated by HRTEM) possesses excellent strain hardening rate and high dislocation storage capacity ($n > 0.45$). As a result, the $Cr_{26}Mn_{20}Fe_{20}Co_{20}Ni_{14}$ HEA exhibits a superior combination of strength and ductility over a wide temperature range of 273-4.2 K.

(2) At 293 K, the YS, UTS and ductility of the $Cr_{26}Mn_{20}Fe_{20}Co_{20}Ni_{14}$ HEA are 145 MPa, 430 MPa and 73%, respectively. The deformation mechanism changes from dislocation slip at initial stage ($\varepsilon = 6\%$) to deformation twinning at mid to late stage ($\varepsilon > 22\%$).

(3) At 203 K, phases transformation happens form FCC to HCP, with a volume fraction of 4.7%. With temperature decrease to 77 K, the lower SFE (9.9 mJ $m^{-2}$) facilitates the formation of abundant twins and induces more phase transformation, enabling the highly-effective-defects (dislocations, twin boundaries and phase interfaces) storage. As a result, the YS, UTS and ductility increase simultaneously to 450 MPa, 1020 MPa, and 95%, respectively.

(4) At 20 and 4.2 K, the deformation behavior is dominated by HCP transformation (30% at 4.2 K), leading to the highest strength and strain hardening rate. The propagation and interaction of the HCP lamellae result in obvious serration behaviors. Thus, the YS and UTS of the $Cr_{26}Mn_{20}Fe_{20}Co_{20}Ni_{14}$ HEA at 4.2 K further increase to 660 MPa and 1300 MPa, respectively, while the ductility decreases to 65% due to plastic instability and premature fracture caused by the severe serration behaviors.

## Declaration of Competing Interest

The authors declare no conflict of interest.

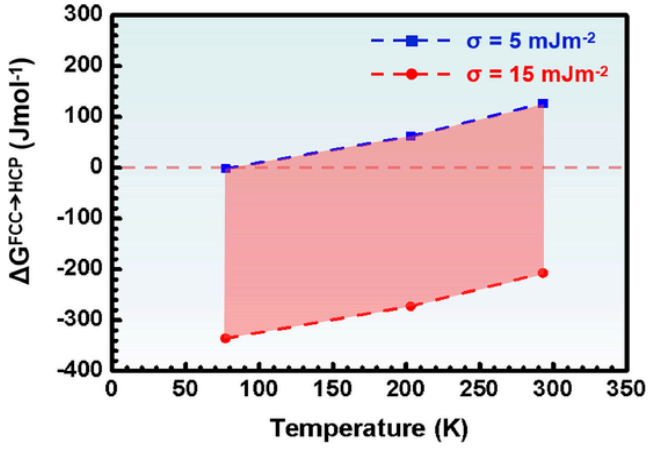


**Fig. 15.** Variation of $\Delta G^{FCC\rightarrow HCP}$ with temperature in the $Cr_{26}Mn_{20}Fe_{20}Co_{20}Ni_{14}$ HEA.

## Acknowledgements

This work was financially supported by the National Key R&D Program of China (Nos. 2021YFA1200203, 2019YFA0209901), the National Natural Science Foundation of China (Nos. 51971112, 51822402 and 51225102), the Fundamental Research Funds for the Central Universities (No. 30919011405), and the LiaoNing Revitalization Talents Program (No. XLYC1807047).

## References

[1] Y. Kimura, T. Inoue, F.X. Yin, K. Tsuzaki, Science 320 (2008) 1057–1060.
[2] B. Gludovatz, A. Hohenwarter, D. Catoor, E.H. Chang, E.P. George, R.O. Ritchie, Science 345 (2014) 1153–1158.
[3] Y. Estrin, N.V. Isaev, S.V. Lubenets, S.V. Malykhin, A.T. Pugachov, V.V. Pustovalov, E.N. Reshetnyak, V.S. Fomenko, L.S. Fomenko, S.E. Shumilin, M. Janecek, R.J. Hellmig, Acta Mater. 54 (2006) 5581–5590.
[4] Z. Wu, H. Bei, G.M. Pharr, E.P. George, Acta Mater. 81 (2014) 428–441.
[5] Z.G. Wu, Y.F. Gao, H.B. Bei, Acta Mater. 120 (2016) 108–119.
[6] Y.M. Wang, E. Ma, R.Z. Valiev, Y.T. Zhu, Adv. Mater. 16 (2004) 328–331.
[7] P. Czarkowski, A.T. Krawczyńska, T. Brynk, M. Nowacki, M. Lewandowska, K.J. Kurzydłowski, Cryogenics 64 (2014) 1–4.
[8] C.S. Zheng, W.W. Yu, Mater. Sci. Eng. A 710 (2018) 359–365.
[9] S.S. Sohn, S. Hong, J. Lee, B.C. Suh, S.K. Kim, B.J. Lee, N.J. Kim, S. Lee, Acta Mater. 100 (2015) 39–52.
[10] B.C. De Cooman, Y. Estrin, S.K. Kim, Acta Mater. 142 (2018) 283–362.
[11] O. Grässel, L. Krüger, G. Frommeyer, L.W. Meyer, Int. J. Plast. 16 (2000) 1391–1409.
[12] B. Cantor, I.T.H. Chang, P. Knight, A.J.B. Vincent, Mater. Sci. Eng. A 375–377 (2004) 213–218.
[13] J.W. Yeh, S.K. Chen, S.J. Lin, J.Y. Gan, T.S. Chin, T.T. Shun, C.H. Tsau, S.Y. Chang, Adv. Eng. Mater. 6 (2004) 299–303.
[14] Z.M. Li, K.G. Pradeep, Y. Deng, D. Raabe, C.C. Tasan, Nature 534 (2016) 227–230.
[15] Z.F. Lei, X.J. Liu, Y. Wu, H. Wang, S.H. Jiang, S.D. Wang, X.D. Hui, Y.D. Wu, B. Gault, P. Kontis, D. Raabe, L. Gu, Q.H. Zhang, H.W. Chen, H.T. Wang, J.B. Liu, K. An, Q.S. Zeng, T.G. Nieh, Z.P. Lu, Nature 563 (2018) 546–550.
[16] B. Gludovatz, A. Hohenwarter, K.V.S. Thurston, H. Bei, Z. Wu, E.P. George, R.O. Ritchie, Nat. Commun. 7 (2016) 10602.
[17] S.B. Wang, M.X. Wu, D. Shu, G.L. Zhu, D.H. Wang, B.D. Sun, Acta Mater 201 (2020) 517–527.
[18] H. Wang, Z.G. Zhu, H. Chen, A.G. Wang, J.Q. Liu, H.W. Liu, R.K. Zheng, S.M.L. Nai, S. Primig, S.S. Babu, S.P. Ringer, X.Z. Liao, Acta Mater. 196 (2020) 609–625.
[19] J.B. Seol, J.W. Bae, J.G. Kim, H. Sung, Z. Li, H.H. Lee, S.H. Shim, J.H. Jang, W.-S. Ko, S.I. Hong, H.S. Kim, Acta Mater. 194 (2020) 366–377.
[20] A.J. Zaddach, C. Niu, C.C. Koch, D.L. Irving, JOM 65 (2013) 1780–1789.
[21] Y.Z. Wang, Z.M. Jiao, G.B. Bian, H.J. Yang, H.W. He, Z.H. Wang, P.K. Liaw, J.W. Qiao, Mater. Sci. Eng. A 839 (2022) 142837.
[22] Q.Z. Mao, Y.S. Zhang, J.Z. Liu, Y.H. Zhao, Nano Lett. 21 (2021) 3191–3197.
[23] J. Glazer, S.L. Verzasconi, R.R. Sawtell, J.W. Morris, Metall. Trans. A 18 (1987) 1695–1701.
[24] R.P. Reed, A.F. Clark, Materials at Low Temperatures, American Society for Metals, Metals Park, OH, 1983, p. 237.
[25] G. Singh, G. Bajargan, R. Datta, U. Ramamurty, Mater. Sci. Eng. A 611 (2014) 45–57.
[26] K.N.T. Ogata, K. Ishikawa, Adv. Cryog. Eng. 40 (1994) 1191–1198.
[27] E.D. Tabachnikova, A.V. Podolskiy, V.Z. Bengus, S.N. Smirnov, M.I. Bidylo, H. Li, P.K. Liaw, H. Choo, K. Csach, J. Miskuf, Mater. Sci. Eng. A 503 (2009) 110–113.
[28] H.Q. Li, P.K. Liaw, H. Choo, E.D. Tabachnikova, A.V. Podolskiy, S.N. Smirnov, V.Z. Bengus, Mater. Sci. Eng. A 493 (2008) 93–96.
[29] K. Han, Y. Xin, R. Walsh, S. Downey, P.N. Kalu, Mater. Sci. Eng. A 516 (2009) 169–179.
[30] E.D. Tabachnikova, A.V. Podolskiy, M.O. Laktionova, N.A. Bereznaia, M.A. Tikhonovsky, A.S. Tortika, J. Alloys Compd. 698 (2017) 501–509.
[31] M.A. Laktionova, E.D. Tabchnikova, Z. Tang, P.K. Liaw, Low Temp. Phys. 39 (2013) 630–632.
[32] N. Nayan, S.V.S. Narayana Murty, A.K. Jha, B. Pant, S.C. Sharma, K.M. George, G.V.S. Sastry, Mater. Des. 58 (2014) 445–450.
[33] Z.B. Xu, H.J. Roven, Z.H. Jia, Mater. Sci. Eng. A 679 (2017) 379–390.
[34] D. Zhemchuzhnikova, A. Mogucheva, R. Kaibyshev, Mater. Sci. Eng. A 565 (2013) 132–141.
[35] D.Y. Li, C.X. Li, T. Feng, Y.D. Zhang, G. Sha, J.J. Lewandowski, P.K. Liaw, Y. Zhang, Acta Mater. 123 (2017) 285–294.
[36] D.Y. Li, Y. Zhang, Intermetallics 70 (2016) 24–28.
[37] Y. Tong, D. Chen, B. Han, J. Wang, R. Feng, T. Yang, C. Zhao, Y.L. Zhao, W. Guo, Y. Shimizu, C.T. Liu, P.K. Liaw, K. Inoue, Y. Nagai, A. Hu, J.J. Kai, Acta Mater. 165 (2019) 228–240.
[38] B.B. Bian, N. Guo, H.J. Yang, R.P. Guo, L. Yang, Y.C. Wu, J.W. Qiao, J. Alloys Compd. 827 (2020) 153981.
[39] K. Wang, X. Jin, Y. Zhang, P.K. Liaw, J.W. Qiao, Phys. Rev. Mater. 5 (2021) 113608.
[40] J.P.H.P.M. Anderson, J. Lothe, Theory of Dislocations, 3rd ed., Cambridge University, New York, USA, 2011, p. 263.
[41] N.L. Okamoto, S. Fujimoto, Y. Kambara, M. Kawamura, Z.M.T. Chen, H. Matsunoshita, K. Tanaka, H. Inui, E.P. George, Sci. Rep. 6 (2016) 35863.
[42] W.J. Lu, C.H. Liebscher, G. Dehm, D. Raabe, Z.M. Li, Adv. Mater. 30 (2018) 1804727.
[43] Z.J. Zhang, M.M. Mao, J.W. Wang, B. Gludovatz, Z. Zhang, S.X. Mao, E.P. George, Q. Yu, R.O. Ritchie, Nat. Commun. 6 (2015) 10143.
[44] A.K. De, D.C. Murdock, M.C. Mataya, J.G. Speer, D.K. Matlock, Scr. Mater. 50 (2004) 1445–1449.
[45] H.L. Huang, Y. Wu, J.Y. He, H. Wang, X.J. Liu, K. An, W. Wu, Z.P. Lu, Adv. Mater. 29 (2017) 1701678.
[46] L. Lu, X. Chen, X. Huang, K. Lu, Science 323 (2009) 607–610.
[47] Y.J. Wei, Y.Q. Li, L.C. Zhu, Y. Liu, X.Q. Lei, G. Wang, Y.X. Wu, Z.L. Mi, J.B. Liu, H.T. Wang, H.J. Gao, Nat. Commun. 5 (2014) 3580.
[48] H. Halim, D.S. Wilkinson, M. Niewczas, Acta Mater. 55 (2007) 4151–4160.
[49] K. Darowicki, J. Orlikowski, A. Zieliński, Mater. Sci. Eng. A 496 (2008) 478–482.
[50] S. Lee, J. Kim, S.J. Lee, B.C. De Cooman, Scr. Mater. 65 (2011) 1073–1076.
[51] S. González, N. Chen, Q.S. Zhang, D.V. Louzguine-Luzgin, J.H. Perepezko, A. Inoue, Scr. Mater. 64 (2011) 713–716.
[52] X.X. Guo, X. Xie, J.L. Ren, M. Laktionova, E. Tabachnikova, L.P. Yu, W.S. Cheung, K.A. Dahmen, P.K. Liaw, Appl. Phys. Lett. 111 (2017) 251905.
[53] F. Otto, A. Dlouhý, C. Somsen, H. Bei, G. Eggeler, E.P. George, Acta Mater 61 (2013) 5743–5755.
[54] V. Shterner, I.B. Timokhina, H. Beladi, Mater. Sci. Eng. A 669 (2016) 437–446.
[55] S. Curtze, V.T. Kuokkala, Acta Mater. 58 (2010) 5129–5141.
[56] T.H. Lee, H.Y. Ha, J.Y. Kang, J. Moon, C.H. Lee, S.J. Park, Acta Mater. 61 (2013) 7399–7410.
[57] J. Miao, C.E. Slone, T.M. Smith, C. Niu, H. Bei, M. Ghazisaeidi, G.M. Pharr, M.J. Mills, Acta Mater. 132 (2017) 35–48.
[58] J. Li, Q.H. Fang, B. Liu, Y. Liu, Acta Mater 147 (2018) 35–41.
[59] P.H. Adler, G.B. Olson, W.S. Owen, Metall. Mater. Trans. A 17 (1986) 1725–1737.
[60] T.Y. Gao, X. Jin, J.W. Qiao, H.J. Yang, Y. Zhang, Y.C. Wu, J. Appl. Phys. 129 (2021) 175101.
[61] Z.M. Li, D. Raabe, JOM 69 (2017) 2099–2106.
[62] Z.J. Zhang, H.W. Sheng, Z.J. Wang, B. Gludovatz, Z. Zhang, E.P. George, Q. Yu, S.X. Mao, R.O. Ritchie, Nat. Commun. 8 (2017) 14390.
[63] D.C. Ma, B. Grabowski, F. Körmann, J. Neugebauer, D. Raabe, Acta Mater. 100 (2015) 90–97.